Research Square

Preprints are preliminary reports that have not undergone peer review.
They should not be considered conclusive, used to inform clinical practice,
or referenced by the media as validated information.

Quantitative Mapping of Hidden Structural Relaxation and Heterogeneity in Sputtered IGZO Thin Films Using 4D-STEM RDF Analysis

Chaeyeon Sim
Ulsan National Institute of Science and Technology
Soobeom Shin
Ulsan National Institute of Science and Technology
Chung Soo Kim
Korea Institute of Ceramic Engineering and Technology
Hu Young Jeong
hulex@unist.ac.kr

Ulsan National Institute of Science and Technology https://orcid.org/0000-0002-5550-5298

Research Article

Keywords:

Posted Date: November 13th, 2026

DOI: https://doi.org/10.21203/rs.3.rs-11457033/v1

License: This work is licensed under a Creative Commons Attribution 4.0 International License.
Read Full License

Abstract

Amorphous indium–gallium–zinc oxide (a-IGZO) is a widely used channel material for thin-film transistors (TFTs), where post-deposition annealing is used to optimize their device performance. However, conventional characterization techniques, such as X-ray diffraction (XRD) and high-resolution transmission electron microscopy (HRTEM), have limited sensitivity to detect the subtle and nanoscale structural evolution, including local atomic rearrangements and nanocrystal nucleation, that precedes macroscopic crystallization and may affect charge transport. To overcome this, we combined four-dimensional scanning transmission electron microscopy (4D-STEM) with spatially resolved radial distribution function (RDF) analysis to map the structural evolution of a-IGZO films as a function of annealing temperature. Although XRD and HRTEM revealed no discernible crystallization up to 500°C, our RDF analysis detected a shift toward shorter distances and a broadening of the metal–oxygen bond distance distribution with increasing annealing temperature, indicating non-uniform local structural relaxation. This nanoscale densification and rearrangement may explain the non-monotonic temperature dependence of the sheet resistance, which decreases up to an annealing temperature of 400°C and increases at higher temperatures. Our 4D-STEM RDF analysis resolves structural dynamics preceding crystallization that remain beyond the detection limits of conventional characterization techniques, thereby providing a new metric to guide process optimization in amorphous oxide semiconductors.

Introduction

a-IGZO is widely employed as a channel material in high-performance TFTs owing to its high carrier mobility and excellent uniformity over large areas. (Nomura et al. 2004; Kamiya and Hosono 2010) Post-deposition thermal annealing is routinely performed to reduce deposition-induced defects and modulate carrier density. (Ide et al. 2019) Although the films remain macroscopically amorphous over a broad temperature range, thermal treatment can induce subtle local structural relaxation, densification, and nanocrystal nucleation. (Sorida et al. 2014; Kim et al. 2009; Huang et al. 2012) Such structural rearrangements preceding crystallization can influence device electrical properties, for example, through the formation of conduction pathways or the introduction of scattering and trapping centers. (Ide et al. 2019) Elucidating and controlling structural evolution preceding crystallization is therefore critical for optimizing annealing processes in amorphous oxide electronics. However, the quantitative characterization of local atomic rearrangements in amorphous thin films remains a significant analytical challenge. Conventional X-ray diffraction (XRD) is primarily sensitive to long-range structural order and provides spatially averaged information over macroscopic sampling volumes, limiting its ability to detect subtle local structural changes before the development of a sufficiently large crystalline volume fraction. (Fewster 2023) Because HRTEM provides a two-dimensional projection of a three-dimensional structure, overlapping structural contributions along the electron-beam direction can obscure sub-nanometer clusters embedded within an amorphous matrix, making them difficult to distinguish from intrinsic phase contrast. (Treacy and Gibson 1996) Therefore, conventional characterization techniques remain largely insensitive to structural evolution occurring during intermediate stages of annealing, prior to macroscopic crystallization. Here, these limitations are addressed by combining 4D-STEM with spatially

resolved RDF analysis. (Lábár et al. 2023; Mu et al. 2019; Mu et al. 2016; Ophus 2019) By recording a two-dimensional diffraction pattern at each scan position and converting it into an RDF, spatially resolved quantitative maps of the local metal–oxygen (M–O) bond distance are obtained across the IGZO films. The analysis reveals the emergence of structural relaxation and spatial heterogeneity at 400°C, although no crystallization is detected by XRD and HRTEM. Furthermore, the nanoscale contraction of the M–O bond distance and the development of local structural heterogeneity are closely correlated with the non-monotonic evolution of the sheet resistance with annealing temperature. By relating nanoscale structural relaxation to macroscopic electrical transport, this study provides a quantitative framework for investigating structural dynamics preceding macroscopic crystallization and for guiding process optimization in amorphous oxide semiconductors.

Results and discussion

Figures 1a, b schematically illustrates the fabrication process with sputter deposition and post-thermal annealing of the a-IGZO films. The a-IGZO films were deposited on SiO_2/Si substrates and subsequently annealed at temperatures ranging from 300 to 600°C in a mixed Ar/O_2 atmosphere with a 3:1 flow ratio. Figure 1c presents the sheet resistance of the a-IGZO thin films as a function of annealing temperature. The sheet resistance exhibits a pronounced non-monotonic, U-shaped dependence, decreasing by approximately three orders of magnitude at 400°C relative to the as-deposited state. This non-monotonic electrical behavior aligns with the annealing-dependent TFT characteristics reported by Suko et al., wherein crystallization initiates at the film surface at 600°C, leading to a decline in field-effect mobility upon extensive crystallization. (Suko et al. 2016)

Grazing-incidence (GI) XRD patterns of the as-deposited and annealed films are presented in Fig. 1d. Films annealed at temperatures up to 500°C exhibit only a broad diffuse feature centered at $2\theta \approx 31–34°$, indicating that they retain an amorphous structure. A distinct diffraction peak emerges at $2\theta \approx 31°$ only after annealing at 600°C and is indexed to the (0009) reflection of rhombohedral $InGaZnO_4$ ($c \approx 26.04$ Å). (Assenmacher et al. 2014) The onset of crystallization at 600°C is consistent with previous reports showing that sputter-deposited a-IGZO with a near-stoichiometric composition crystallizes at approximately 600°C. (Suko et al. 2016) Specifically, Suko et al. reported that DC-sputtered a-IGZO remains amorphous after annealing at temperatures up to 300°C, whereas annealing at 600°C induces surface-initiated crystallization with a preferential c-axis orientation. (Suko et al. 2016) Cross-sectional HRTEM images (Figs. 1e-g) provide further insight into the microstructural evolution observed by XRD. The as-deposited and 400°C-annealed films exhibit featureless image contrast and diffuse halo rings in the corresponding fast Fourier transform (FFT) patterns, confirming an amorphous matrix. After annealing at 600°C, a crystalline layer approximately 4.33 nm thick is observed at the film surface, whereas the underlying region retains amorphous contrast. Lattice fringes with a spacing of 0.287 nm are resolved within this surface layer and are oriented parallel to the film surface. This spacing agrees well with the (0009) interplanar spacing of $InGaZnO_4$ ($d_{0009} \approx 0.289$ nm). (Assenmacher et al. 2014) The orientation of these lattice fringes indicates preferential alignment of the c-axis normal to the film surface, consistent with the (0009) dominant texture observed by XRD and with previous reports of

surface-initiated crystallization in an IGZO film. Preferential nucleation at the free surface can be attributed to reduced kinetic constraints relative to the film interior, as reported for other amorphous systems. (Suko et al. 2016; Assenmacher et al. 2014; Zhu et al. 2008) The reduction in film thickness observed in the cross-sectional HRTEM images is consistent with thermally activated densification, whereby annealing below the crystallization temperature promotes structural relaxation and reduces the excess free volume incorporated during sputter deposition. (Troughton et al. 2017; Egami et al. 1980) Accordingly, substantial densification occurs at annealing temperatures up to 500°C, although the associated local atomic rearrangements within the amorphous matrix cannot be resolved by conventional XRD and HRTEM. To probe local short-range order, 4D-STEM measurements were performed by scanning a nanometer-sized electron probe across the specimen while recording a two-dimensional diffraction pattern at each probe position. Electron-diffraction-based RDF analysis has recently emerged as an effective approach for mapping short- and medium-range structural order in amorphous and mixed amorphous–nanocrystalline materials with a spatial resolution of a few nanometers. (Kang et al. 2024) This approach was employed to quantify the temperature-dependent evolution of the mean M–O bond distance on a pixel-by-pixel basis. (Kang et al. 2014)

The overall analysis workflow is summarized in Fig. 2. For each diffraction pattern, the direct beam center was determined on a frame-by-frame basis using its center of mass, and defective detector pixels were masked. The corrected pattern was then azimuthally averaged to obtain a one-dimensional intensity profile, I(s). The atomic scattering background was modeled as $I(s) = N\langle f^2(s)\rangle + C$ using tabulated electron-scattering factors weighted according to the film composition. The reduced intensity function was subsequently calculated as $\varphi(s) = s[I(s) - N\langle f^2\rangle - C]/N\langle f\rangle^2$. Residual low-frequency baseline contributions were removed using a constrained polynomial fit, and the corrected φ(s), was damped and sine-transformed to generate a spatially registered g(r) data cube across the scanned region. The first peak in g(r), corresponding to the nearest-neighbor M–O coordination shell, was fitted with a pseudo-Voigt function over the range of 1.7–2.3 Å. (Young and Wiles 1982) The resulting peak positions were then mapped to generate the atomic bond-distance maps shown in Fig. 3. Two methodological considerations are important for interpreting these maps. First, although the real-space resolution constrains the absolute width of individual g(r) peaks, peak positions resolved via pseudo-Voigt fitting retain high precision, enabling a robust statistical analysis of their spatial distribution. (Young and Wiles 1982) Second, because the diffraction signal at each scan position is integrated through the film thickness, the resulting maps represent thickness-averaged bond distances. Detailed procedures for dataset processing and the Fourier-transform parameters are provided in the Methods.

Figure 3 presents the virtual bright-field (VBF) images, corresponding M–O bond-distance maps, and pixel-wise bond-distance distributions for the as-deposited, 400°C-annealed, and 600°C-annealed a-IGZO thin films. These data reveal two systematic trends in the local structure with increasing annealing temperature. First, the M–O bond distance decreases monotonically with increasing annealing temperature. The mean M–O bond distance decreases from 2.100 Å in the as-deposited film to 2.007 Å after annealing at 400°C, and further to 1.986 Å at 600°C. The overall decrease of 0.114 Å across the annealing series is substantially greater than the spatial standard deviation measured in the as-

deposited film (σ = 0.025 Å), indicating a significant shift. This bond distance contraction is consistent with the dissipation of excess free volume incorporated during deposition through thermally activated structural relaxation, resulting in densification of the atomic network. (Kamiya and Hosono 2010; Troughton et al. 2017; Egami et al. 1980) Furthermore, the nanoscale contraction in M–O bond distance aligns with the macroscopic reduction in film thickness measured by HRTEM (Figs. 1e–g), providing complementary evidence for densification across multiple length scales. Second, the local structure becomes heterogeneous across the film with increasing annealing temperature. The spatial standard deviation of the extracted M–O correlation distance increases more than threefold, from 0.025 Å in the as-deposited film to 0.090 Å after annealing at 600°C. Accordingly, the bond-distance distributions broaden and become increasingly asymmetric, with a progressively more pronounced tail extending toward longer distances. Because identical acquisition conditions and fitting procedures were applied to all datasets, the contribution of fitting uncertainty to the measured spatial dispersion is negligible across the annealing series. The observed broadening therefore reflects increased spatial heterogeneity in the local structure rather than a systematic deterioration in measurement precision. The origin of the observed local structural heterogeneity differs between the intermediate and high-temperature annealing regimes. At 400°C, where both XRD and HRTEM show no detectable crystallinity due to their detection limits, nanoscale regions characterized by shorter M–O correlation distances coexist with relatively unrelaxed regions in a spatially heterogeneous network. This spatial variation reflects heterogeneous structural relaxation, wherein thermally driven densification proceeds non-uniformly across the amorphous matrix. (Orita et al. 2000; Ide et al. 2012) These more strongly relaxed localized regions may represent structural features preceding crystallization, suggesting that an early structural response to annealing occurs as nanoscale spatial fluctuations in local order, well before the onset of XRD-detectable crystallinity. By contrast, the pronounced spatial heterogeneity observed across the map at 600°C originates from the coexistence of two distinct structural phases within the cross-section: the newly formed surface crystalline layer and the underlying amorphous matrix. Rather than a transmission-overlap effect at individual scan positions, the pixel-wise aggregation of M–O bond distances across the entire cross-sectional map captures both the highly relaxed/ordered surface layer and the residual amorphous interior. The coexistence of these two regions broadens and skews the overall M–O distance distribution. Collectively, these results demonstrate that 4D-STEM-based RDF analysis enables quantitative mapping of pre-crystallization structural relaxation and its nanoscale fluctuations, resolving early-stage structural evolution that remains inaccessible to conventional XRD and HRTEM.

The electrical response in Fig. 1c correlates with the two-stage structural evolution revealed by our 4D-STEM RDF analysis. Along the descending branch, from the as-deposited state to 400°C, the sheet resistance decreases by approximately three orders of magnitude. Across this temperature range, our RDF analysis reveals a systematic shift of the first coordination-shell peak toward shorter distances, consistent with local network contraction and structural relaxation. Previous studies have suggested that structural relaxation in a-IGZO can modulate oxygen-vacancy-related defect states and promote the conversion of oxygen vacancies into shallow-donor states as excess free volume is reduced. (Hong et al. 2026) This interpretation aligns with the pronounced decrease in sheet resistance observed here, while

our RDF results provide a corresponding nanoscale structural signature of this annealing-induced relaxation. Along the ascending branch, the increase in sheet resistance becomes evident at 500°C, preceding the crystallization detectable by XRD and HRTEM, and becomes substantially more pronounced at 600°C. This increase in sheet resistance may reflect the progressive development of local structural heterogeneity associated with the onset of crystallization. The reversal in electrical behavior originates from distinct mechanisms at different annealing stages. The initial increase in sheet resistance at 500°C is likely driven by thermally activated modification or passivation of oxygen-related defect states, whereas the more pronounced rise at 600°C stems from severe carrier scattering and trapping at crystalline–amorphous interfaces and grain boundaries within the surface nanocrystalline layer. (Suko et al. 2016; Moffitt et al. 2023) Collectively, these findings suggest that substantial changes in electrical transport are closely linked to nanoscale structural relaxation and local heterogeneity within the nominally amorphous regime. In the present system, the minimum sheet resistance is attained following local structural densification within the amorphous phase, whereas further annealing promotes the development of more pronounced nanocrystalline regions and crystalline–amorphous interfaces, potentially introducing additional carrier-scattering pathways. This mechanistic framework provides a structural basis for optimizing annealing conditions in amorphous oxide semiconductors.

Conclusions

In summary, this study establishes a spatially resolved 4D-STEM-based RDF analysis framework to quantify nanoscale short-range order evolution in a-IGZO thin films during thermal annealing. By tracking the first-shell M–O RDF peak position at each scan position, this approach resolves two key structural features beyond the detection limits of XRD and HRTEM: progressive local M–O bond contraction and the emergence of spatial heterogeneity. Furthermore, these structural findings suggest a nanoscale mechanism underlying the non-monotonic temperature dependence of sheet resistance. The decrease in sheet resistance up to 400°C coincides with structural relaxation and local densification within the amorphous network, whereas the subsequent increase from 500°C can be further associated with changes in oxygen-related defect states and, at 600°C, additional carrier scattering and trapping associated with grain boundaries and crystalline-amorphous interfaces. The relative contributions of these mechanisms require further investigation through complementary spectroscopic and transport measurements. More generally, the spatially resolved 4D-STEM RDF framework can be extended to investigate nanoscale structure-property relationships in materials that remain macroscopically amorphous. By enabling the direct visualization and quantification of structural evolution preceding crystallization and nanoscale heterogeneity, our approach provides a robust basis for investigating processing-structure-property relationships and for optimizing thermal processing in amorphous oxide semiconductors.

Experimental section

Film deposition and annealing:

a-IGZO thin films were deposited on thermally oxidized SiO_2/Si substrates at room temperature by radio-frequency (RF) magnetron sputtering using a ceramic $InGaZnO_4$ target with a nominal cation ratio of In:Ga:Zn = 1:1:1. Before deposition, the sputtering chamber was evacuated to a base pressure below 6.0 × 10^{-4} Pa. Sputtering was performed at an RF power of 80 W under an Ar flow of 25 sccm at a working pressure of 0.45 Pa for 1 min 40 s. The chemical composition of the as-deposited film was confirmed using energy-dispersive X-ray spectroscopy (EDS) to be In:Ga:Zn ≈ 1:1:1.

Thermal annealing was performed in a tube furnace under a controlled Ar/O_2 atmosphere at a working pressure of 3.5 × 10^{-1} Torr. The samples were heated at a ramp rate of 10°C min^{-1} to target temperatures ranging from 300 to 600°C, held at the target temperature for 1 h, and subsequently cooled naturally to room temperature under continuous gas flow. The annealing atmosphere consisted of Ar and O_2 gas flows of 60 and 20 sccm, respectively. (Yeon et al. 2016)

Structural characterization

The crystallinity of the films was examined by grazing-incidence X-ray diffraction (GIXRD) using a SmartLab diffractometer (Rigaku) equipped with a 9 kW rotating Cu anode (Cu Kα, λ = 1.5406 Å), parallel-beam optics incorporating a parabolic mirror, and a hybrid multi-channel semiconductor detector in a θ–θ vertical goniometer geometry. Measurements were performed at a fixed grazing incidence angle (ω) of 0.5° over a 2θ range of 20–60°, with a step size of 0.01° and a scan speed of 1° min^{-1}.

Cross-sectional specimens for transmission electron microscopy (TEM) were prepared using a focused ion beam (FIB) lift-out technique with a Helios 450HP dual-beam system (Thermo Fisher Scientific) employing a Ga^+ ion beam. Final thinning and cleaning were performed at a low accelerating voltage (2 kV) to minimize surface amorphization and ion-beam-induced damage. To remove the Ga^+-damaged surface layer and suppress Ga redeposition or clustering introduced during FIB milling, the specimens were subsequently polished by low-energy Ar^+ ion milling using a Fischione Model 1040 NanoMill system (700 eV, 210 μA). High-resolution transmission electron microscopy (HRTEM) imaging and fast Fourier transform (FFT) analysis were performed using a JEM-ARM300F microscope (JEOL) operated at 300 kV. Film thicknesses were measured directly from cross-sectional HRTEM images.

4D-STEM acquisition

4D-STEM datasets were acquired using a JEM-ARM300F microscope (JEOL) operated at 300 kV with an 80 cm camera length. Diffraction patterns were recorded using a Gatan OneView camera with a detector size of 256 × 256 pixels and an exposure time of 0.05 s per frame. The electron probe was configured with a semi-convergence angle of α = 1.456 mrad. The 2D scan raster comprised 400 × 34 probe positions across the cross-sectional specimen. The spatial step size was set to 1.0 nm with a dwell time of 0.05 s. Reciprocal-space calibration was performed using diffraction patterns acquired from a single-crystal silicon (110) reference substrate under identical electron-optical conditions.

RDF analysis and bond-distance mapping

RDFs were calculated from the 4D-STEM datasets using an in-house Python-based analysis pipeline built on NumPy (Harris et al. 2020), SciPy (Virtanen et al. 2020), and HyperSpy (de la Peña et al. 2023). For each diffraction pattern, the direct-beam center was determined from the intensity-weighted center of mass of the central disk, and defective detector pixels were masked. The diffraction pattern was subsequently azimuthally averaged about the fitted beam center to obtain the one-dimensional intensity profile, I(s), after excluding the low-angle region dominated by the direct beam.

The atomic scattering background was modeled as $I(s) = N\langle f^2(s)\rangle + C$, where the electron scattering factors were calculated using Kirkland's four-term Gaussian–Lorentzian parameterization and weighted according to the nominal film composition (In:Ga:Zn = 1:1:1). The scale factor N and offset C were determined by fitting the high-s region of I(s), yielding the reduced intensity function, $\varphi(s) = s\cdot[I(s) - N\langle f^2\rangle - C]/(N\langle f\rangle^2)$, where $\langle f^2\rangle$ and $\langle f\rangle^2$ represent the composition-weighted mean-square and squared mean scattering factors, respectively. Following residual baseline correction and application of a damping envelope to suppress termination ripples, φ(s) was sine-transformed according to $g(r) = 8\pi \int \varphi(s) \sin(2\pi sr)\, ds$, generating a spatially registered g(r) data cube corresponding to the VBF image.

For bond-distance mapping, the first g(r) peak at each scan position, corresponding predominantly to the nearest-neighbor M–O coordination shell, was fitted using a pseudo-Voigt profile. The fitted peak center was extracted as a local descriptor of the characteristic M–O correlation distance. The distributions of fitted peak positions across all valid pixels were summarized by their mean, and standard deviation.

Electrical characterization

The sheet resistance of the as-deposited and annealed films was measured by the four-point probe (4PP) method with a commercial sheet resistance measurement system (CMT-100, AIT Co., Ltd.) equipped with a Jandel four-point probe head. Measurements were performed at room temperature (approximately 24°C) over an applied current range of 10 nA to 100 mA.

Declarations

Competing interests

The authors declare that they have no competing interests

Funding

This work was supported by the National Strategic Reference Materials Program (RS-2025-14323015) and the Korea Institute for Advancement of Technology (KIAT) grant (P0023703, HRD Program for Industrial Innovation) funded by the Ministry of Trade, Industry and Resources (MOTIR).

Author Contributions

C.S. deposited and annealed the IGZO films, performed the XRD and four-point-probe measurements, and analyzed the HRTEM and 4D-STEM data. S.S. assisted with the HRTEM and 4D-STEM measurements. H.Y.J. conceived the idea, supervised the project, and reviewed the manuscript.

Acknowledgements

This work was supported by the National Strategic Reference Materials Program (RS-2025-14323015) and the Korea Institute for Advancement of Technology (KIAT) grant (P0023703, HRD Program for Industrial Innovation) funded by the Ministry of Trade, Industry and Resources (MOTIR).

Data availability

The datasets generated during the current study are available from the corresponding author on reasonable request.

References

1. K. Nomura, H. Ohta, A. Takagi, T. Kamiya, M. Hirano, H. Hosono, Nature. **432**, 488 (2004)
2. T. Kamiya, H. Hosono, NPG Asia Mater. **2**, 15 (2010)
3. K. Ide, K. Nomura, H. Hosono, T. Kamiya, Phys. Status Solidi A **216**, 1800372 (2019)
4. N. Sorida, M. Takahashi, K. Dairiki, S. Yamazaki, N. Kimizuka, Jpn J. Appl. Phys. **53**, 115501 (2014)
5. G.H. Kim, B.D. Ahn, H.S. Shin, H.J. Kim, H.J. Kim, J. Electrochem. Soc. **156**, H7 (2009)
6. Y.C. Huang, P.Y. Yang, H.Y. Huang, S.J. Wang, H.C. Cheng, J. Nanosci. Nanotechnol. **12**, 5625 (2012)
7. P.F. Fewster, Crystals. **13**, 521 (2023)
8. M.M.J. Treacy, J.M. Gibson, Acta Crystallogr. A **52**, 212 (1996)
9. J.L. Lábár, K. Hajagos-Nagy, P.P. Das, A. Gomez-Perez, G. Radnóczi, Nanomaterials. **13**, 3136 (2023)
10. X. Mu, A. Mazilkin, C. Sprau, A. Colsmann, C. Kübel, Microscopy. **68**, 301 (2019)
11. X. Mu, D. Wang, T. Feng, C. Kübel, Ultramicroscopy. **168**, 1 (2016)
12. C. Ophus, Microsc Microanal. **25**, 563 (2019)
13. T. Suko, M. Takahashi, T. Onuki, N. Ishihara, J. Koyama, S. Yamazaki, Jpn J. Appl. Phys. **55**, 035504 (2016)
14. W. Assenmacher, S. Mader, A. Mader, R. Glaum, M. Binnewies, J. Solid State Chem. **215**, 176 (2014)
15. L. Zhu, L. Wong, L. Yu, Mol. Pharm. **5**, 921 (2008)
16. J.G. Troughton, P. Downs, R. Price, D. Atkinson, Appl. Phys. Lett. **110**, 011903 (2017)
17. T. Egami, K. Maeda, V. Vitek, Philos. Mag A **41**, 883 (1980)
18. S. Kang, B. Hwang, C. Kim, H. Kim, J. Park, S. Kim, S. Hwang, Acta Mater. **263**, 119495 (2024)
19. Y. Kang, H. Song, H.H. Nahm, S.H. Jeon, Y. Cho, S. Han, APL Mater. **2**, 032108 (2014)

20. R.A. Young, D.I. Wiles, J. Appl. Crystallogr. **15**, 430 (1982)
21. M. Orita, H. Tanji, M. Mizuno, H. Adachi, I. Tanaka, Phys. Rev. B **61**, 1811 (2000)
22. K. Ide, K. Nomura, H. Hiramatsu, T. Kamiya, H. Hosono, J. Appl. Phys. **111**, 073513 (2012)
23. S.L. Moffitt, Q. Ma, E.A. Weiss, M.J. Bedzyk, T.J. Marks, J. Phys. Chem. C **127**, 23099 (2023)
24. S. Hong, I. Oh, J. Park, Y. Kim, S. Lee, H. Kim, Solid-State Electron. **235**, 109368 (2026)
25. H.W. Yeon, S.M. Choi, B.S. Kim, H.J. Kim, NPG Asia Mater. **8**, e250 (2016)
26. C.R. Harris, K.J. Millman, S.J. van der Walt, R. Gommers, P. Virtanen, D. Cournapeau, E. Wieser, J. Taylor, S. Berg, N.J. Smith, R. Kern, M. Picus, S. Hoyer, M.H. van Kerkwijk, M. Brett, A. Haldane, J.F. del Río, M. Wiebe, P. Peterson, P. Gérard-Marchant, K. Sheppard, T. Reddy, W. Weckesser, H. Abbasi, C. Gohlke, T.E. Oliphant, Nature 585, 357 (2020)
27. P. Virtanen, R. Gommers, T.E. Oliphant, M. Haberland, T. Reddy, D. Cournapeau, E. Burovski, P. Peterson, W. Weckesser, J. Bright, S.J. van der Walt, M. Brett, J. Wilson, K.J. Millman, N. Mayorov, A.R.J. Nelson, E. Jones, R. Kern, E. Larson, C.J. Carey, İ. Polat, Y. Feng, E.W. Moore, J. VanderPlas, D. Laxalde, J. Perktold, R. Cimrman, I. Henriksen, E.A. Quintero, C.R. Harris, A.M. Archibald, A. Ribeiro, F. Pedregosa, P. van Mulbregt, SciPy 1.0 Contributors, Nat. Methods. **17**, 261 (2020)
28. F. de la Peña, E. Prestat, V.T. Fauske, P. Burdet, P. Jokubauskas, M. Nord, T. Ostasevicius, K.E. MacArthur, M. Sarahan, D.N. Johnstone, J. Taillon, A. Eljarrat, V. Migunov, J. Caron, T. Aarholt, S. Mazzucco, T. Slater, F. Winkler, P.S. M, B. Martineau, G. Donval, R. McLeod, E.R. Hoglund, I. Alxneit, D. Lundeby, T. Henninen, Zagonel, A. Gorenstein, HyperSpy, Zenodo (2023)

Figures

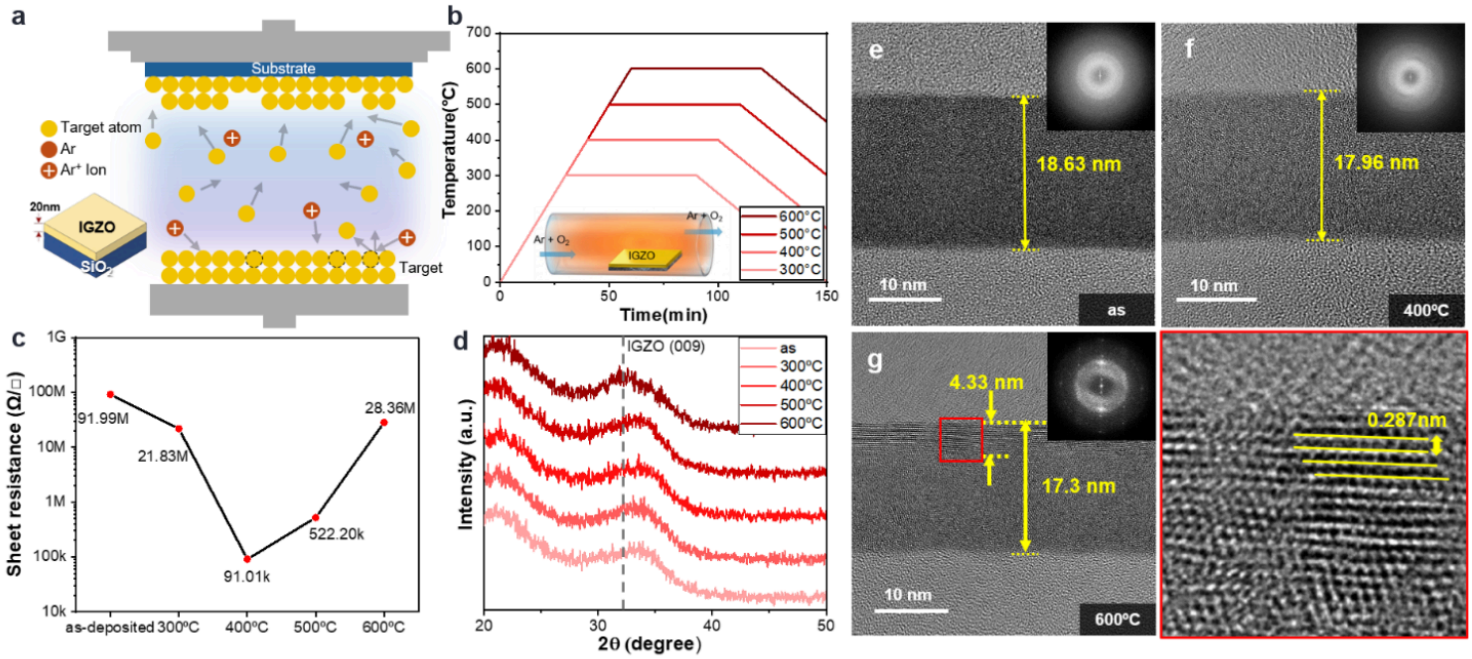


Figure 1

Processing schematics and microstructural evolution of a-IGZO thin films. a, Schematic illustration of the IGZO thin film sputtering process. **b,** The corresponding heat treatment temperature profiles and schematic of the tube furnace for Ar/O_2 atmosphere annealing (inset). **c**, Sheet resistance of the IGZO thin films as a function of annealing temperature. **d,** GIXRD patterns of IGZO thin films as a function of annealing temperature. Representative cross-sectional HRTEM images and corresponding FFT patterns (inset) for **e,** as-deposited, **f,** 400 °C-annealed, and **g,** 600 °C-annealed IGZO thin films, revealing a preferentially c-axis oriented crystalline surface layer at 600 °C with an interplanar spacing of approximately 0.287 nm.

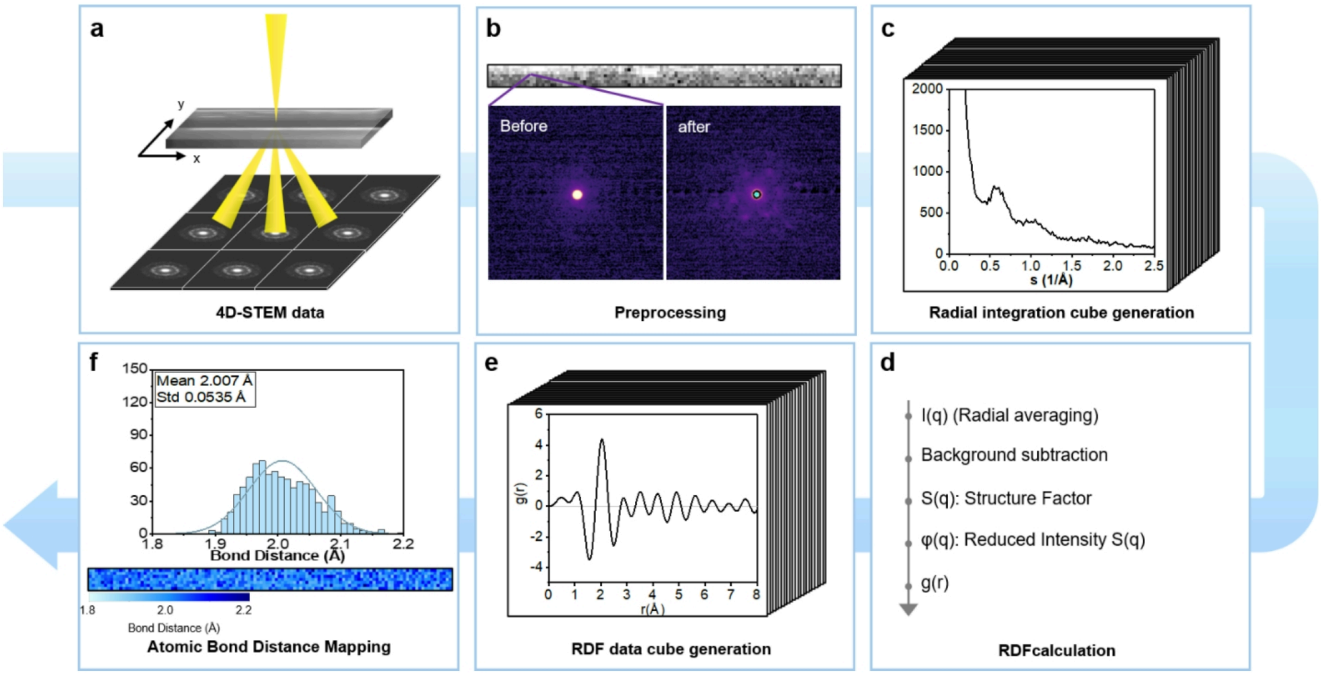


Figure 2

4D-STEM RDF analysis workflow and mapping procedure. Schematic illustration showing **a,** 4D-STEM data acquisition, **b,** diffraction pattern preprocessing, **c,** azimuthal integration to generate a data cube, **d,** RDF calculation from the integrated profiles, **e,** construction of the spatially registered RDF data cube, and **f,** quantitative atomic bond-distance mapping.

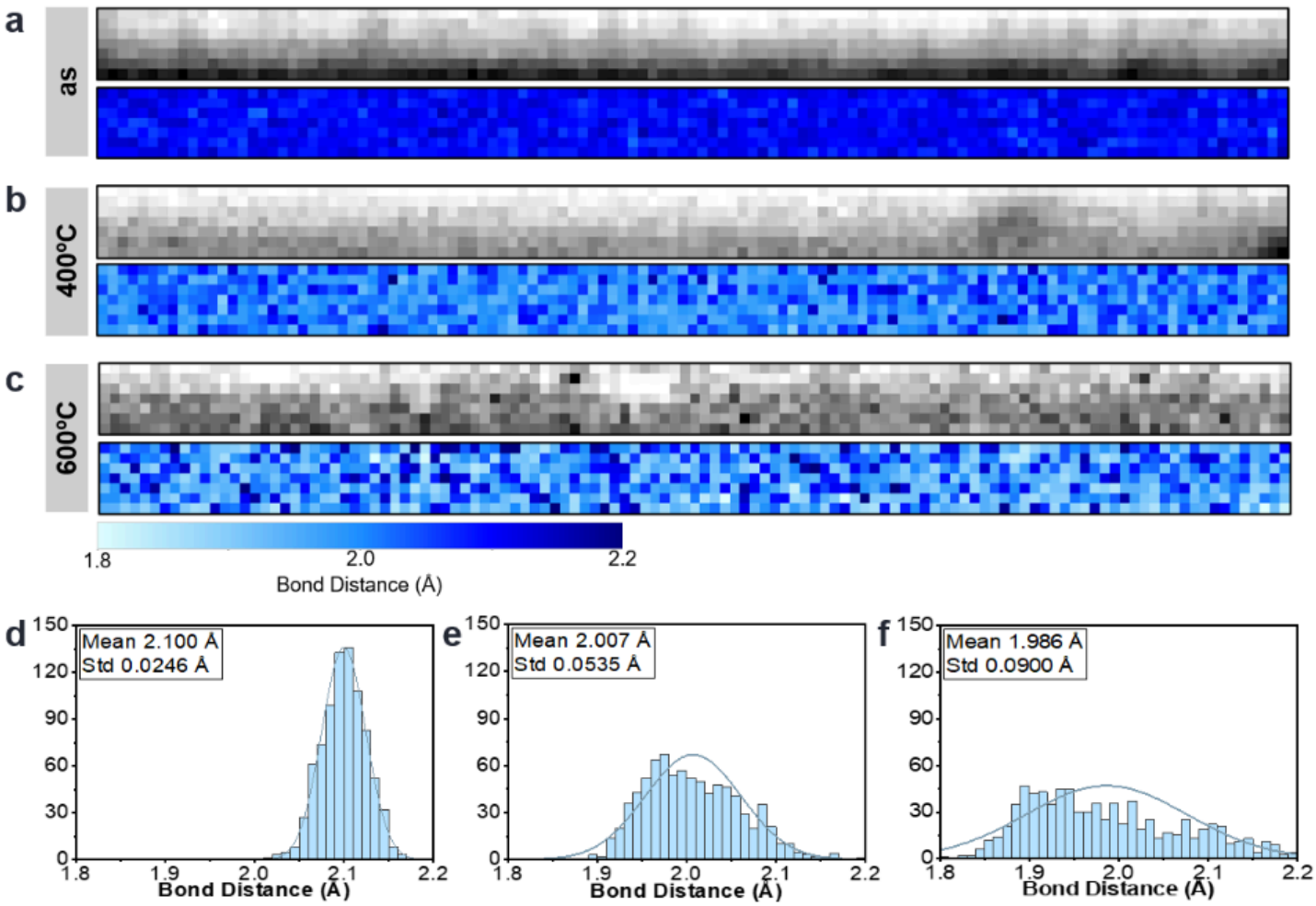


Figure 3

Spatially resolved M–O bond-distance maps and statistical distributions as a function of annealing temperature. a–c, Virtual bright-field STEM images (upper panels)and corresponding M–O bond-distance maps (lower panels) for **a,** as-deposited, **b,** 400 °C-annealed, and **c,** 600 °C-annealed a-IGZO thin films. The color scale represents the M–O bond distance ranging from 1.8 to 2.2 Å. **d–f,** Corresponding statistical histograms and fitted distributions of local M–O bond distances for **d,** as-deposited**, e,** 400 °C-annealed, and **f,** 600 °C-annealed samples. Higher annealing temperatures induce a contraction in the mean M–O bond distance accompanied byincreased spatial heterogeneity.